

Generalized hydraulic geometry: Insights based on fluvial instability analysis and a physical model

Boyko Dodov and Efi Foufoula-Georgiou

St. Anthony Falls Laboratory and National Center for Earth-Surface Dynamics, Department of Civil Engineering, University of Minnesota, Minneapolis, Minnesota, USA

Received 19 March 2004; revised 9 September 2004; accepted 28 September 2004; published 9 December 2004.

[1] The power law dependencies between channel morphology and river flows, known as at-station hydraulic geometry (HG), have been recently shown to have exponents that systematically vary with scale (contributing area). To explain these empirical trends, a generalized HG model whose parameters are explicit functions of scale was derived by *Dodov and Foufoula-Georgiou* [2004], based on a statistical multiscaling formalism. In this paper we attempt to provide a physical explanation for this scale dependence. The hypothesis we pose is that it arises from the scale dependence of fluvial instability, which induces systematic variation in river planform geometry (e.g., sinuosity, meander wavelength, and radius of curvature) and consequent variations in channel cross-sectional shape with scale. In other words, we postulate that the scale-dependent HG is a direct consequence of the systematic increase of channel cross-sectional asymmetry over reaches of increasing scale. To test this hypothesis, we employ both a direct analysis of observations and also a physical model of meandering rivers, which is based on linearization of the fully coupled equations of mass and momentum balance for water and sediment. We show that the HG emerging from this physical model is scale-dependent and agrees with the empirical observations and the statistical multiscaling model. *INDEX TERMS*: 1824 Hydrology: Geomorphology (1625); 1860 Hydrology: Runoff and streamflow; 1821 Hydrology: Floods; *KEYWORDS*: channel asymmetry, floods, fluvial instability, hydraulic geometry, scaling

Citation: Dodov, B., and E. Foufoula-Georgiou (2004), Generalized hydraulic geometry: Insights based on fluvial instability analysis and a physical model, *Water Resour. Res.*, 40, W12201, doi:10.1029/2004WR003196.

1. Introduction

[2] Hydraulic geometry (HG) refers to the power laws relating stream width W , average depth D , and mean velocity V to discharge Q : $W = aQ^b$, $D = cQ^d$, $V = kQ^m$ [*Leopold and Maddock*, 1953]. These relationships have been observed to hold either for different discharges at an individual cross section (referred to as at-station HG), or for different downstream locations related through some characteristic discharge, e.g., mean annual discharge (referred to as downstream HG). This paper is concerned with the at-station HG.

[3] In a recent paper, *Dodov and Foufoula-Georgiou* [2004] presented empirical evidence that the exponents of at-station HG systematically depend on scale, i.e., drainage area upstream (A), and showed that this empirical trend can be captured by a multiscaling formalism of hydraulic geometry factors. Specifically, they postulated and confirmed via analysis of observations that the probability distributions of discharge Q and cross-sectional area C_A remain statistically invariant under proper rescaling with a random function which depends on scale only (notion of multiscaling). As a result, lognormal multiscaling models were fitted to Q and C_A and revised at-station HG relation-

ships (i.e., relationships between C_A and Q and V and Q) whose coefficients were explicit functions of scale, were derived. These relationships were called generalized HG and were tested on 85 stations in Oklahoma and Kansas with good agreement to observations.

[4] In this paper, we attempt to provide a physical explanation of the empirically observed and statistically described scale dependence of at-station HG in terms of downstream variations in fluvial instability. First, we briefly review the multiscaling formalism of HG that gives rise to generalized at-station HG relationships. Then, we present an analysis of fluvial instability [*Parker*, 1976] as a function of contributing area to show that channel planform geometry (e.g., sinuosity, curvature and wavelength) and, particularly, the transition between straight and meandering channels, are scale-dependent. To relate channel planform geometry and channel shape, we use the model of *Johannesson and Parker* [1987, 1989] to calculate the bed topography of representative meander bends of a given Strahler order, and then, the HG of these bends. This model is based on a small perturbation approach which linearizes the governing equations maintaining full coupling between the flow field, bed load transport and bed topography. We show that the at-station HG that emerges from this physical model is scale-dependent and agrees with the empirical trends and the proposed statistical model. We also show by direct analysis of observations that the velocity HG exponent depends inversely on

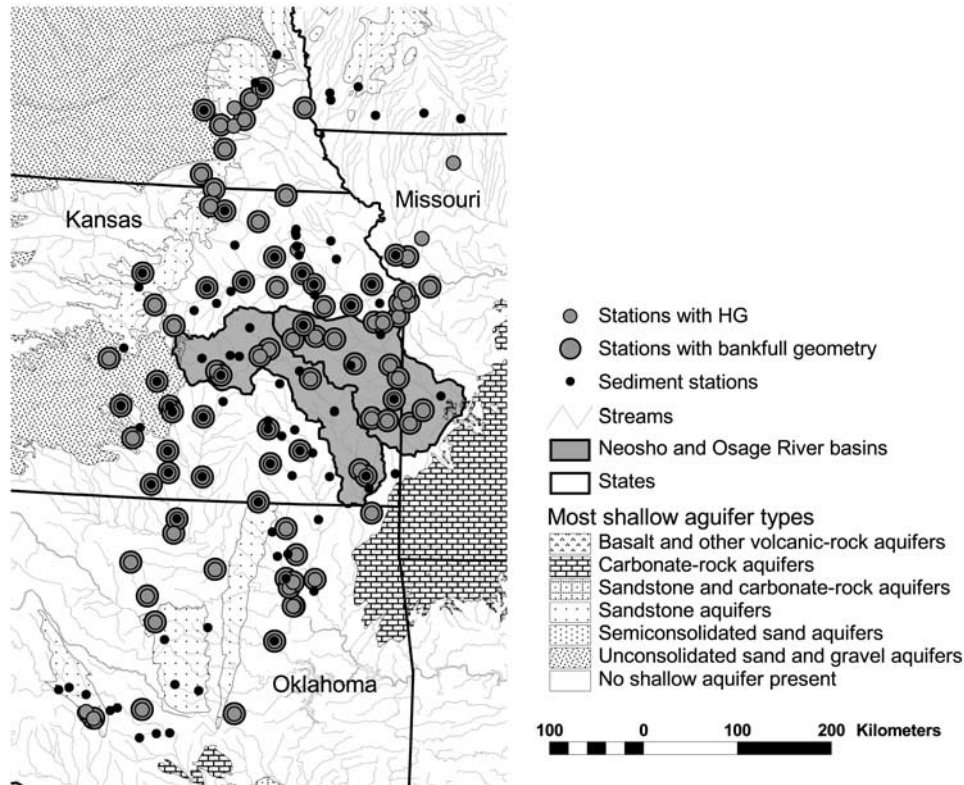


Figure 1. Locations of the 96 stations of data set A and the 92 stations of data set C. The shaded basins are shown in more detail in Figure 2.

channel sinuosity and that sinuosity increases as a function of scale. These results together with findings from the physical model are interpreted as evidence that the physical origin of the scale-dependent HG is the systematic increase of channel asymmetry downstream induced by scale-dependent fluvial instability.

2. Data Sets

[5] The data used in this study consist of the following sets.

2.1. Data Set A

[6] Ninety-six stations in Nebraska, Kansas, Missouri and Oklahoma (see Figure 1) consisting of: (a) independent measurements of width, mean depth, cross-sectional area, mean velocity and discharge under different flow conditions (up to several hundred measurements per station) allowing computation of at-station HG as well as determination of channel bank-full discharge and geometry (Q_{bf} , W_{bf} , D_{bf} and V_{bf}) for 92 of the stations, (b) channel slopes for 64 of the stations and (c) time series of at least 3 years of unregulated daily discharges for 74 of the stations. Gages were chosen such that they are located in a similar elevation band. Also, the climatic conditions and underlying geology of the considered drainage basins are similar such that pronounced heterogeneities due to external factors are avoided. The upstream and downstream channel properties of more than two hundred stations were carefully examined through

analysis of satellite images, aerial photographs and topographic maps 1:24,000 to choose the 96 stations that do not have channel corrections upstream from the station. Consequently, this data set is a bit different than the one used by *Dodov and Foufoula-Georgiou* [2004].

2.2. Data Set B

[7] High-resolution hydrography data (U.S. Geological Survey National Hydrography Data Set (NHDS)) for Neosho and Osage river basins in Kansas and Missouri (see Figure 2). These data are available in a vector format (polylines consisting of sequences of $[X, Y]$ pairs of practically infinite resolution) allowing representation of curvatures with radius of order $O(1$ to 10 m) which is impossible to derive from elevation raster data (usually available at resolution of 30 m). 21 out of the 96 stations of data set A are located in Neosho and Osage river basins.

[8] It is noted that regulations do not affect the analysis based on data set A and B (i.e., computation of at-station HG and extraction of channel cross-sectional and planform geometries) since changes in channel geometry due to regulations have been found insignificant except immediately downstream of a dam [e.g., see *Juracek*, 1999, 2000].

2.3. Data Set C

[9] Data from 92 stations in Nebraska, Iowa, Kansas, Missouri consisting of independent measurements of suspended sediment load and suspended sediment concentration under different flow conditions (up to several hundred measurements per station) with at least 3 years of unregu-

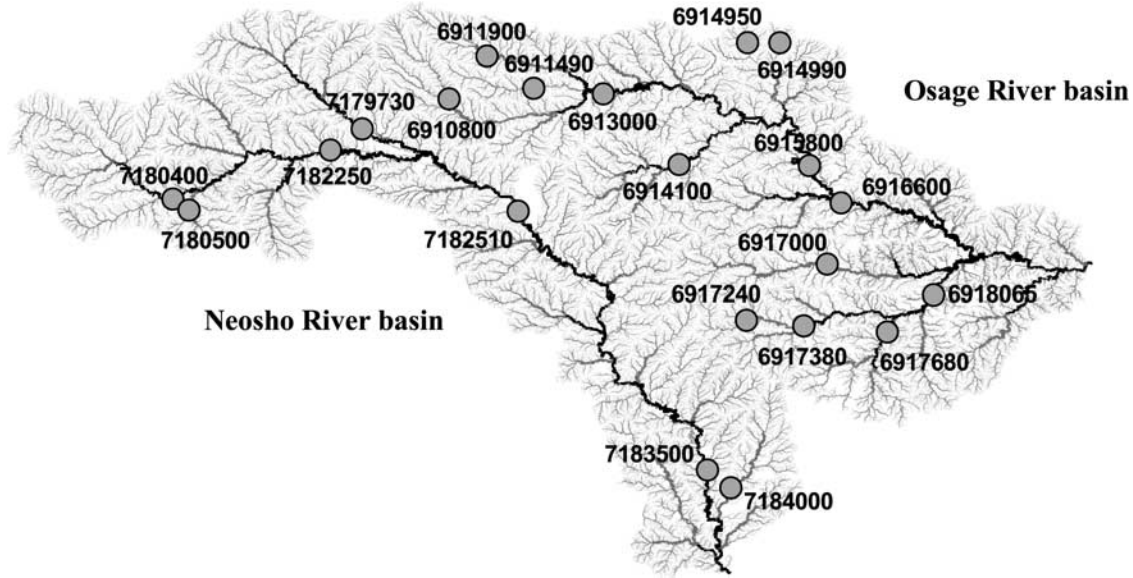


Figure 2. River network represented by high-resolution hydrography of data set B and the 21 stations of data set A located in the Neosho and Osage river basins.

lated record. 32 of the stations are common for data sets A and C (see Figure 1).

3. Review of Generalized At-Station HG

[10] Evidence was presented by *Dodov and Foufoula-Georgiou* [2004], based on 85 stations located in a geologically and climatologically homogeneous region in Oklahoma and Kansas, that the parameters (exponents and preexponents) of at-station HG have a systematic dependence on scale. For example, the at-station HG for velocity $V = kQ^m$ was empirically fitted to the 85 stations and estimates of the parameters k and m were plotted as a function of scale A (see points in Figure 3). In the same figure estimates of the parameter m for Sangamon river basin (approximately 500 km east-northeast from Osage river basin) as given by *Stall and Fok* [1968] are also shown. A trend of decrease of the exponent m with scale is apparent, indicating an increase in the “linearity” of catchment response as the contributing area increases (i.e., less dependence of velocity on discharge as m tends to zero). At the same time, it was observed that the exponents of downstream HG depend on the frequency of discharge [see *Dodov and Foufoula-Georgiou*, 2004, Figure 7].

[11] To explain these empirical findings, a multiscaling framework was proposed within which processes whose spatial variability changes as a function of scale and frequency can be concisely and parsimoniously described. Specifically, it was postulated that the discharge Q and channel cross-sectional area C_A obey multiscaling lognormal (MSL) models whose p th quantiles are of the form

$$\ln C_{Ap}(A) = (\alpha_{C_A} + \beta_{C_A} \ln A) + (\gamma_{C_A} + \delta_{C_A} \ln A)^{1/2} z_p \quad (1a)$$

$$\ln Q_p(A) = (\alpha_Q + \beta_Q \ln A) + (\gamma_Q + \delta_Q \ln A)^{1/2} z_p,$$

$$\text{for } A_l^0 < A < A_l^1, \quad (1b)$$

where $\alpha_{(\cdot)}$, $\beta_{(\cdot)}$, $\gamma_{(\cdot)}$ and $\delta_{(\cdot)}$ are parameters, z_p is a standard normal quantile, A is the contributing area, and A_l^0 and A_l^1 represent some limiting contributing areas within which the scaling behavior holds (see *Dodov and Foufoula-Georgiou* [2004] and also the original papers of *Gupta and Waymire* [1990] and *Gupta et al.* [1994] for more details on the multiscaling theory). The above multiscaling models were fitted to the 85 stations in Oklahoma and Kansas (see *Dodov and Foufoula-Georgiou* [2004] for the details of fitting; 10 quantiles of the PDFs of Q and C_A of all 85 stations were fitted simultaneously through least squares) and the parameters of the multiscaling models of (1a)–(1b) were estimated and are shown in Table 1.

[12] Since power law relationships on lognormal random variables result in preservation of quantiles, equations (1a)–(1b) can be combined in order to determine scale-dependent at-station relationships between C_A , V and Q similar to the *Leopold and Maddock* [1953] power laws:

$$C_{Ap} = \Phi_{C_A}(A) Q_p^{\Psi_{C_A}(A)} \quad (2a)$$

$$V = \Phi_V(A) Q^{\Psi_V(A)}, \quad (2b)$$

where

$$\Psi_{C_A}(A) = \left(\frac{\gamma_{C_A} + \delta_{C_A} \ln A}{\gamma_Q + \delta_Q \ln A} \right)^{1/2}, \quad (3a)$$

$$\Phi_{C_A}(A) = \exp[(\alpha_{C_A} + \beta_{C_A} \ln A) - (\alpha_Q + \beta_Q \ln A) \Psi_{C_A}(A)], \quad (3b)$$

$$\Psi_V(A) = 1 - \Psi_{C_A}(A), \quad (3c)$$

$$\Phi_V(A) = 1/\Phi_{C_A}(A) \quad (3d)$$

(see *Dodov and Foufoula-Georgiou* [2004] for details).

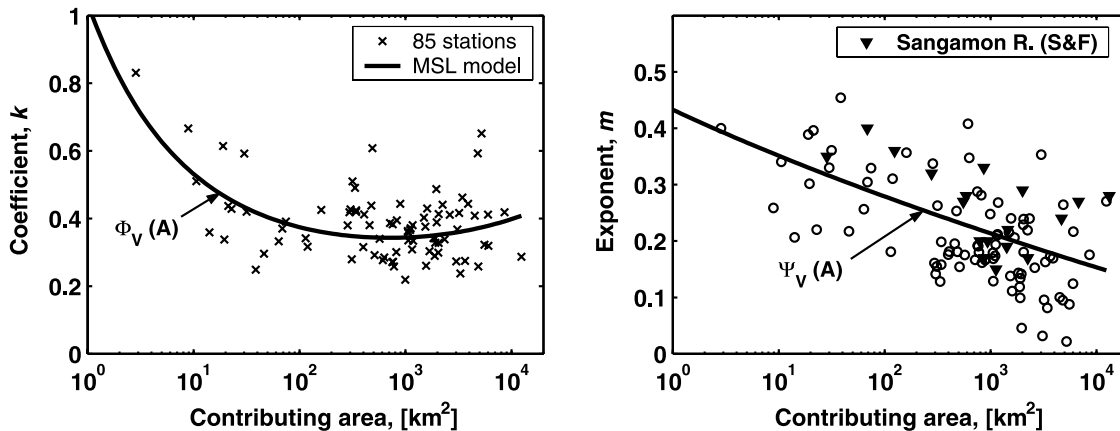


Figure 3. Points indicating the (left) at-station exponents and (right) preexponents for velocity hydraulic geometry (HG) (i.e., parameters of the fitted *Leopold and Maddock* [1953] power law $V = kQ^m$) for the 85 stations in Oklahoma and Kansas analyzed by *Dodov and Foufoula-Georgiou* [2004] versus their contributing area. Lines indicate the theoretical curves $\Phi_V(A)$ and $\Psi_V(A)$ derived from the multiscaling model (equations(3a)–(3d)). The results of *Stall and Fok* [1968] for the Sangamon River are also given for comparison (reproduced from the values of Table 8 of their report) (adapted from *Dodov and Foufoula-Georgiou* [2004, Figure 15]).

[13] In Figure 3 the theoretical curves $\Phi_V(A)$ and $\Psi_V(A)$ computed from equations (3a)–(3d) using the multiscaling parameters of Table 1 are plotted. We see that these theoretical curves are in good agreement with the observations validating thus the proposed multiscaling model for HG.

4. Systematic Downstream Variation in Channel Planform Geometry and Cross-Sectional Asymmetry: The Effect of Scale-Dependent Fluvial Instability

[14] Channel cross-sectional shape can be easily shown to have a significant effect on the HG of an idealized channel. For example, consider two channels: one with wide rectangular and the other with triangular (asymmetric or symmetric) cross section. Using Manning’s relation for velocity $V \sim C_A^{2/3} P^{-2/3}$, (for the same Manning’s n and channel slope, where C_A is the cross-sectional area and P is the wetted perimeter) it can be shown that the HG exponent for velocity is 0.4 for the wide rectangular channel and 0.25 for the triangular channel. Considering that the transition from a straight to a meandering channel consists of a combination of almost rectangular to trapezoidal to asymmetric triangular cross sections (e.g., see *Johannesson and Parker* [1987, 1989] for details), and the observation that meandering induces asymmetry in the cross sections of natural rivers (as evidenced by *Leopold and Wolman* [1960], who site that approximately 90% of meandering channels have asymmetric cross sections), a possible connection seems to emerge as to whether the scale dependence of HG is due to the systematic increase of channel asymmetry downstream induced by scale dependence in river planform geometry. In particular, we pose and answer the following two questions: (1) how and why does the sinuosity of meandering rivers change with scale, and (2) how does the degree of sinuosity affect the channel cross section asymmetry and in general the HG?

The first question is addressed in this section and the second question in section 5.

[15] The transition between the three characteristic fluvial morphologies of channels (meandering, braiding, and straight) has been considered by *Parker* [1976] based on stability analysis of a two-dimensional alluvial river model previously proposed by *Hansen* [1967] and *Callander* [1969]. The approach is based on a perturbation technique, involving a small parameter representing the ratio of sediment transport to water transport. *Parker* [1976] derived an instability criterion ϵ^*

$$\epsilon^* = SW/\pi FrD, \tag{4}$$

where S is the along-channel slope and W , Fr and D are respectively the width, the Froude number and the mean depth at formative discharges (usually assumed bank-full ones), which can be used to differentiate between the three regimes. The theory indicates that if the depth to width ratio $D/W \ll 1$ and sediment transport is present (conditions which are usually satisfied in natural rivers) a tendency toward either meandering or braiding exists. Meandering occurs for $S/Fr \ll D/W$, braiding occurs for $S/Fr \gg D/W$ and transition between the two regimes occurs if $S/Fr \approx D/W$. Thus if $\epsilon^* \ll 1$ meandering occurs, if $\epsilon^* \gg 1$

Table 1. Parameters of the Fitted Lognormal Multiscaling Models for Cross-Sectional Area and Discharge^a

Hydraulic Geometry Factors	Estimated Model Parameters			
	α	β	γ	δ
<i>D&FG, 85 Stations</i>				
Cross-sectional area, C_A	-3.18	0.61	0.84	0.1130
Discharge, Q	-5.54	0.81	2.61	0.0012
<i>This Study, 80 Stations</i>				
Cross-sectional area, C_A	-3.44	0.69	1.11	0.0581
Discharge, Q	-6.00	0.90	3.00	-0.0721

^aSee equations (1a) and (1b).

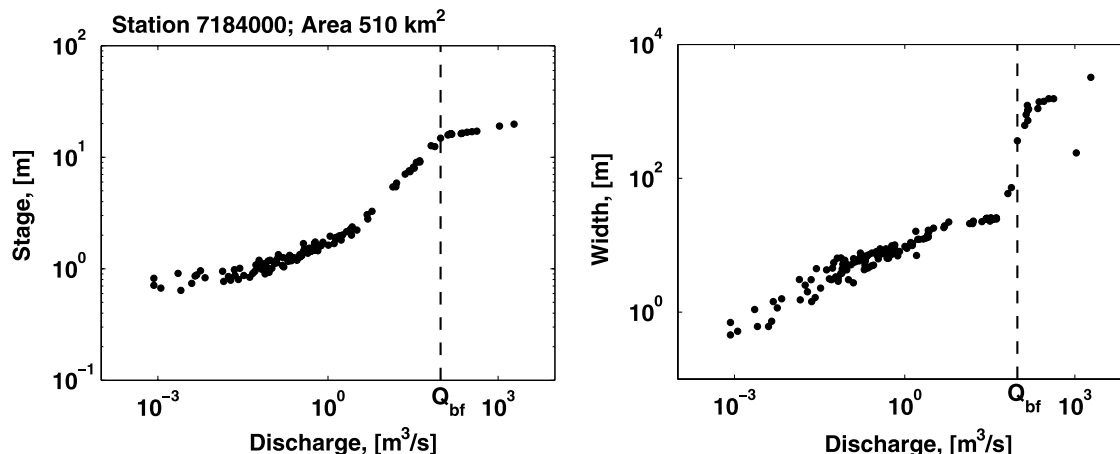


Figure 4. An example of determination of bank-full discharge.

braiding occurs (with a number of braids $n_{br} \sim \varepsilon^*$) and if $\varepsilon^* = O(1)$ transition between meandering and braiding is present. The condition for the maintenance of straight channels is assumed to be $D/W > 0.1$.

[16] In the work of *Parker* [1976] no consideration of scale was made and inferences, about flow instabilities and transition from one regime to another, were made irrespectively of whether channels drained a small or a large upstream area. In our work, we use the available data (data sets A and B) to perform a stability analysis as a function of scale.

[17] In order to apply stability analysis, we first need to determine the bank-full discharge Q_{bf} , width W_{bf} , average depth D_{bf} and mean velocity V_{bf} for all available stations based on the empirical stage-discharge and width-discharge relationships. Bank-full conditions were considered to occur when a break in slope was observed in both stage-discharge and width-discharge relationships (a transition to a very slow increase in stage and very rapid increase in width after bank-full discharge is reached). An example of determination of bank-full discharge is given in Figure 4. The width, mean velocity, mean depth and cross-sectional area at bank-full were obtained from the nearest measurement below the break. In some cases, where Q_{bf} was determined using only stage and discharge data (i.e., no data for W , V , etc. were available at around bank-full discharges), W_{bf} , V_{bf} and D_{bf} were obtained by eye from the corresponding log-log plots versus discharge Q . The bank-full channel geometries and discharge for the 92 stations of data set A (for which these properties were determined) are presented in Figure 5 as a function of contributing area (scale). In the same figure, the at-station local channel slopes S and the ratio D_{bf}/W_{bf} needed for stability analysis are also given as a function of scale.

[18] The observations (points) in Figure 5 suggest some trends in the bank-full properties with scale. Specifically, it is noted that W_{bf} , D_{bf} and Q_{bf} versus scale can be well described by double log-log linear relationships which exhibit a break at a scale of approximately 700 km². The solid lines shown for these variables in Figure 5 were fitted by eye keeping the scale of transition from one log-log linear relationship to the other equal to 700 km² as clearly dictated by the W_{bf} , D_{bf} and Q_{bf} relationships. The dashed lines in the V_{bf} and D_{bf}/W_{bf} versus area plots were derived from the fitted lines of W_{bf} , D_{bf} and Q_{bf} . The solid line in the

relationship of along-channel slope S versus contributing area was fitted by eye with no assumed break using the available at-station local slopes and the information extracted from the Digital Elevation Models (DEM) of Neosho and Osage river basins.

[19] Once we have obtained the channel morphometry parameters at bank-full as a function of scale we can proceed with the stability analysis described above. In Figure 6a we plot the ε^* criterion at bank-full computed from (4) versus scale for the 64 stations of data set A for which the at-station along-channel slopes were available. The fact that ε^* is almost constant for scales up to ~ 700 km² suggests that sinuosity should be almost constant for streams that drain areas up to that scale. However, the plot of S/Fr_{bf} versus D_{bf}/W_{bf} in Figure 6b shows that for medium to small scales (~ 700 km² to 10 km²) the ratio D_{bf}/W_{bf} approaches values greater than 0.1 (from below) implying transition from moderate meandering to straight channels as the contributing area decreases. In contrast, for scales larger than ~ 700 km², ε^* decreases with contributing area which suggests increase in fluvial instability with scale. At the same time, the plots of D_{bf}/W_{bf} versus contributing area and S/Fr_{bf} versus D_{bf}/W_{bf} show that the ratio D_{bf}/W_{bf} is almost constant with scale implying suppressed instability for scales of order larger than $O(1000$ km²). It is noted that the broken line in Figure 6a and the arrows in Figure 6b are computed from the log-linear approximations in Figure 5.

[20] Considering the fact that the sinuosity can be used as a descriptor of fluvial instability for $\varepsilon^* \ll 1$, the overall inference from the above analysis is that moderate sinuosity should be observed at scales of order $O(1000$ km²), a trend for slight decrease of sinuosity with increase in contributing area should be present at larger scales, and almost straight channels (sinuosity converging to 1) should dominate at scales less than approximately 100 km².

[21] To independently check the above conclusion, we performed an analysis of the high-resolution hydrography data set for the Neosho and Osage river basins (data set B). The data set was first carefully examined to clean all loops and artificial channels (where possible) in order to assign a particular Strahler stream order to every channel in the river network. Then the sinuosity, meander wavelength and channel slope were computed separately for every bend using simultaneous analysis of vector and elevation raster

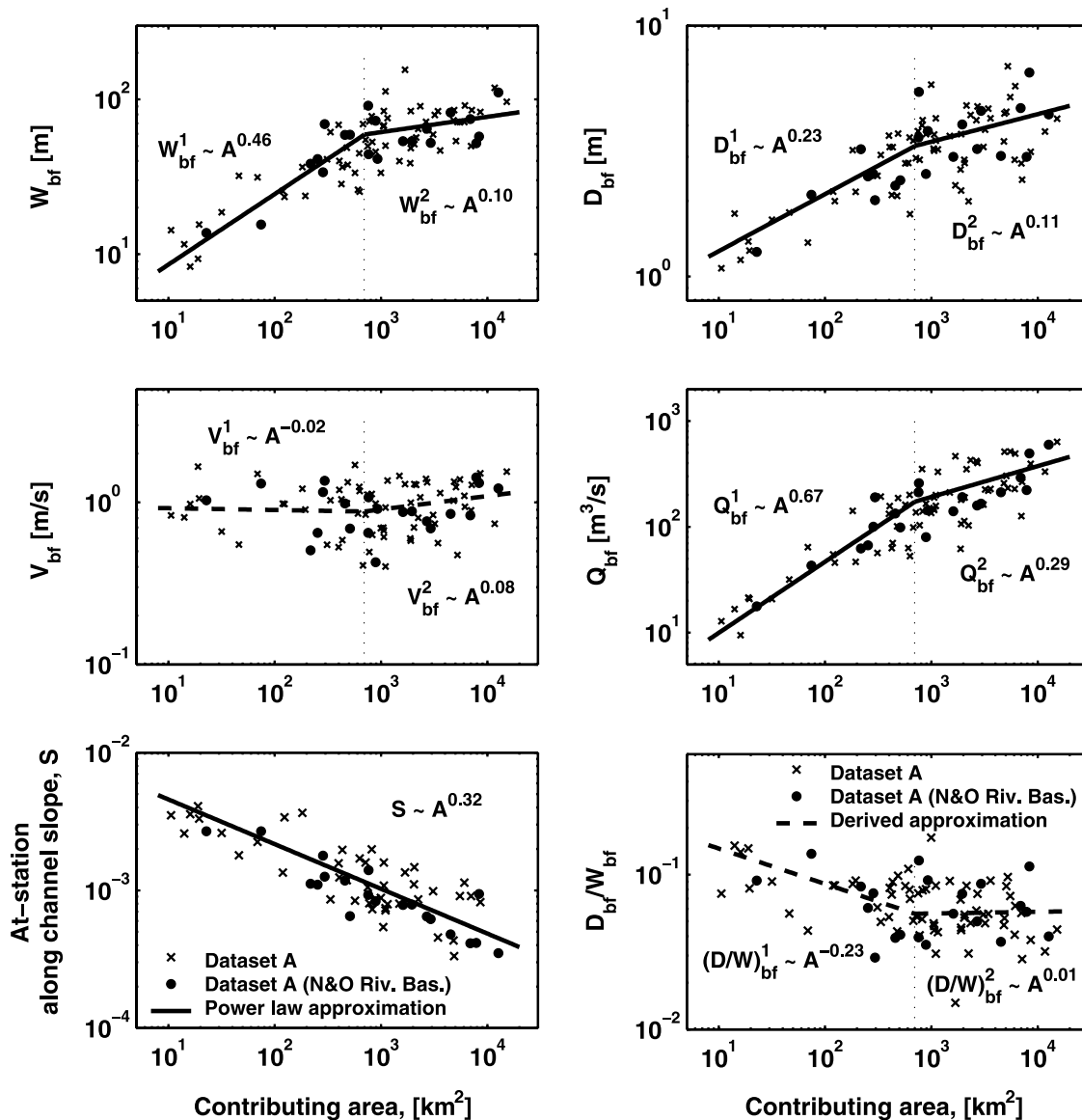


Figure 5. Dependence of the parameters of bank-full morphometry and at-station channel slope on scale (contributing area). Crosses represent data set A and circles represent the stations of data set A located in Neosho and Osage river basins. At-station along-channel slopes were available for data set B and for 64 stations from data set A. Solid lines correspond to relationships fitted directly to the observations, and dashed lines correspond to derived relationships.

data. (Technical details about the definition of the meander bend and the estimation of sinuosity, meander wavelength, minimum radius of curvature for a given channel bend are given in Appendix A).

[22] The analysis of planform geometry showed that the distributions of the above parameters for a given stream order are nonsymmetric (e.g., approximately lognormal for meander wavelength and power law distribution for sinuosity, e.g., see an example in Figure 7). This is why, in our analysis it was considered more appropriate to use medians rather than means as representative estimates of these parameters:

Median meander wavelength

$$\lambda_{\omega}^{med} = \text{Med}[\lambda_{\omega}^i] \quad (5a)$$

Median sinuosity

$$s_{\omega}^{med} = \text{Med}[s_{\omega}^i], \quad (5b)$$

where λ_{ω}^i and s_{ω}^i are respectively the wavelength and sinuosity of an individual meander bend of order ω .

[23] If a meander bend is assumed to follow a sine-generated curve (a common assumption in fluvial geomorphology), approximate estimates of other descriptors of meander planform geometry can be derived. These parameters (used in our analysis later on) are the minimum radius of curvature of the bend $R_{\min} \approx \lambda [(s-1)/s]^{-1/2}/4.4\pi$ and its angle amplitude $\Theta_O \approx 2.2[(s-1)/s]^{1/2}$ (see *Langbein and Leopold* [1966] and *Johannesson and Parker* [1989] for details). As could be expected, for bends of a given

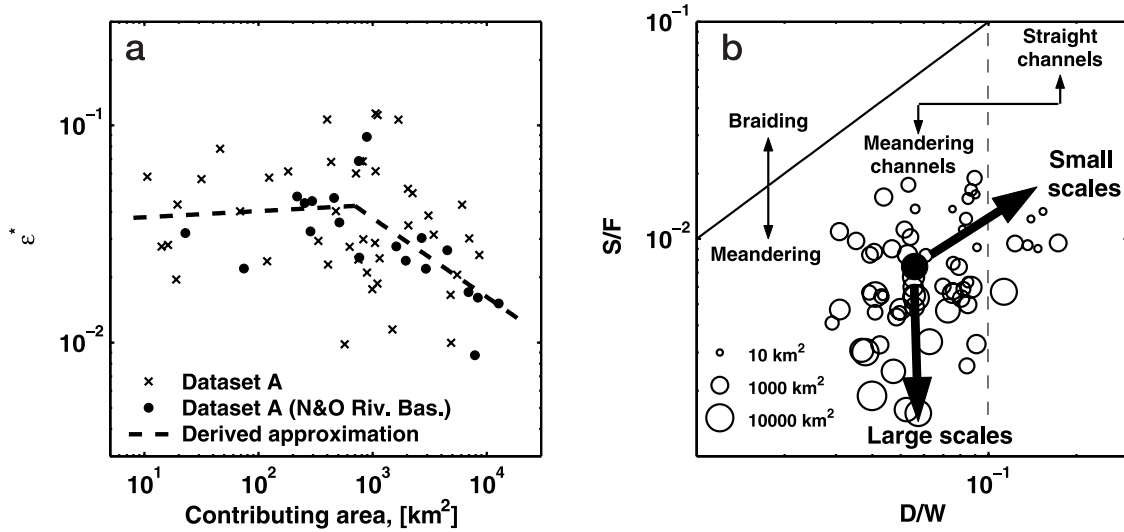


Figure 6. (a) Channel stability criterion as a function of scale. (b) Transition from meandering to straight channels with contributing area (see text for explanation).

order the minimum radius of curvature and the angle amplitude also followed nonsymmetric distributions and, respectively, their median values were considered representative values of these parameters:

Median angle amplitude

$$\Theta_O^{\omega,med} \approx 2.2 \text{Med} \left\{ \left[(s_\omega^i - 1) / s_\omega^i \right]^{1/2} \right\} \quad (6a)$$

Median of the minimum radius of curvature

$$R_{min}^{\omega,med} \approx \text{Med} \left\{ \lambda_\omega^i \left[(s_\omega^i - 1) / s_\omega^i \right]^{-1/2} \right\} / 4.4\pi. \quad (6b)$$

[24] The estimated values of the parameters in (5a)–(5b) and (6a)–(6b) are given in Table 2 grouped according to channel’s stream order and are also plotted in Figure 8. Note that channel stream order relates monotonically to contributing area as shown in Figure 8d and therefore, area and stream order are used interchangeably in the rest of the paper.

[25] The results clearly support the prediction from stability analysis, i.e., maximum (but moderate, 1.30) median sinuosity is observed at streams of order 6 ($\sim 1000 \text{ km}^2$), decreasing median sinuosity with an increase of scale to streams of order 8 ($\approx 10,000 \text{ km}^2$) and approach to almost

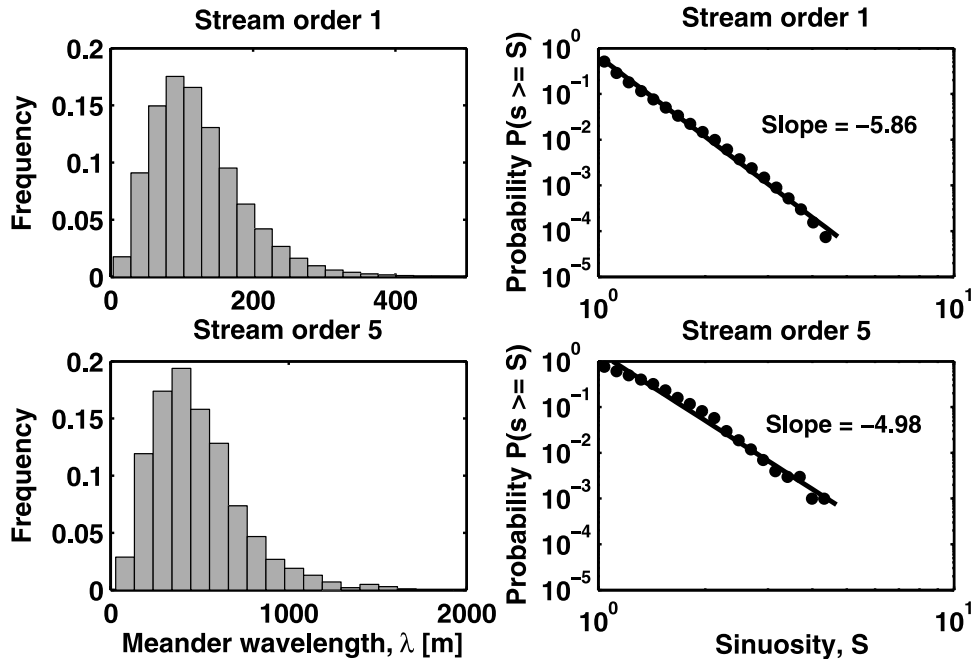


Figure 7. (left) Sample probability density functions (PDFs) of meander wavelength and (right) cumulative probability functions of sinuosity for streams of order 1 and 5 from data set B. The nonsymmetric nature of the PDFs is noted with approximately lognormal for the meander wavelength and power law for sinuosity. Similar PDFs were found for other-order streams.

Table 2. Median Parameters of Channel Cross-Sectional and Planform Geometry for Meander Bends of Order ω Used as an Input to the Model of *Johannesson and Parker* [1987, 1989]^a

Order ω	Area A , km ²	Mean Velocity V_{bf} , m s ⁻¹	Mean Depth D_{bf} , m	Channel Slope S	Half-width b_{bf} , m	Wavelength λ , m	Perturbation Parameter ψ_0	Sinuosity s	Angle Amplitude Θ_0 , rad	Minimum Radius of Curvature R_{min} , m	Number of Bends
1	0.4	0.95	0.61	0.01286	1.00	112.5	0.034	1.09	0.62	24.7	161,219
2	2.8	0.93	0.95	0.00690	2.41	129.7	0.090	1.15	0.80	24.0	44,618
3	11.6	0.92	1.31	0.00436	4.58	175.0	0.136	1.19	0.89	31.2	16,769
4	52.9	0.90	1.84	0.00266	9.15	258.9	0.193	1.22	0.94	45.3	5562
5	220.9	0.89	2.55	0.00167	17.54	442.0	0.226	1.26	1.00	74.2	1007
6	989.4	0.90	3.44	0.00103	30.69	604.7	0.306	1.30	1.05	97.4	983
7	7087.2	1.06	4.27	0.00054	37.30	1018.5	0.208	1.25	0.98	168.7	692
8	14,581.2	1.13	4.62	0.00043	40.06	1848.0	0.116	1.26	1.00	305.2	31

^aStream orders, median contributing areas, and parameters describing meander planform geometry are prototyped based on the Neosho and Osage river basins (data set B). The channel slope and morphometry parameters at bank-full are obtained from the relationships in Figure 5 (data set A) for the appropriate contributing areas A_ω .

straight channels (median sinuosity 1.09) at streams of order 1 (≈ 1 km²). This agreement between empirical observations and physical theory is satisfying and provides insight into the physical origin of the empirically observed scale-dependent sinuosity in natural rivers (Figure 8c) in terms of fluvial instability (Figure 6).

[26] Although the analysis of fluvial instability (based on the variation of channel properties with scale) supports the increase of channel sinuosity in the downstream direction, there is another factor that strongly affects channel cross-sectional shape and planform geometry, namely, the sedi-

ment supply regime (see *Leopold and Wolman* [1957], *Schumm and Khan* [1972], and *Ikeda* [1989], among others). Particularly, in their paper *Schumm and Khan* [1972] reported results from flume experiments in which they observed that a change in the suspended sediment load rapidly increased sinuosity and transverse slope of the experimental channel. This observation suggests that if there is a trend of increase in channel sinuosity with scale, such a trend might be related to a change in sediment supply regime in the downstream direction, the existence of which would be an additional support to our conclusions. To check

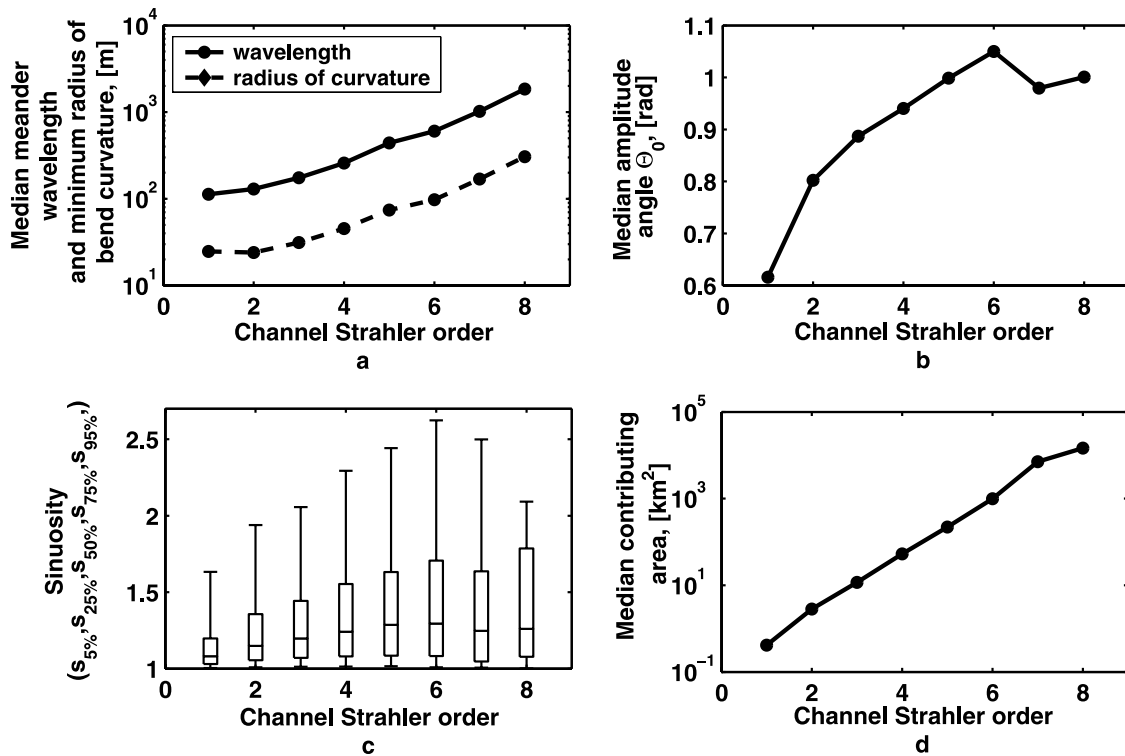


Figure 8. Parameters of meandering derived from the high-resolution hydrography data of the Neosho and Osage river basins (data set B) as a function of Strahler order or scale (see the relation of the two at the bottom right plot). The sinuosity plot shows the median sinuosity and the 5%, 25%, 75%, and 95% quantiles. An increase not only in the median but also in the variability of sinuosity with scale is observed from that plot.

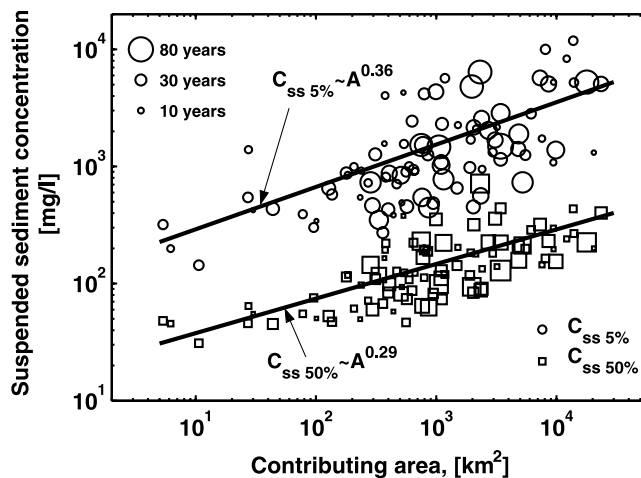


Figure 9. Suspended sediment concentrations corresponding to two quantiles of water discharge (probability of exceedance 50% and 5%) as a function of scale. Water discharge quantiles and the corresponding suspended sediment concentrations are extracted from at least 3 years of unregulated flows at the daily scale.

if the sediment supply regime does change with contributing area we analyzed the suspended sediment concentration at different flow conditions for the 92 stations of data set C. In Figure 9 we plot the suspended sediment concentration corresponding to frequency of exceedance of daily discharges 50% and 5% in order to consider two quantiles below bank-full conditions. It is seen that both quantiles follow approximately straight lines with slopes respectively 0.29 and 0.36 in log-log space. This overall trend of an increase in suspended sediment concentration with scale for below bank-full conditions is, according to *Schumm and Khan [1972]*, another physically based motivation to assume that the sinuosity increases in the downstream direction.

[27] Having established the dependence of channel planform geometry on scale, in the next section we continue with the next important step in our analysis, namely, to provide a connection between the increasing sinuosity and the parameters of at-station hydraulic geometry. It is noted that establishing a direct (observation-based) connection between channel sinuosity and channel cross section asymmetry is practically infeasible as channel cross section data over many reaches with different contributing areas do not exist. Such a connection can only be inferred using a physical model of water and sediment transport, and this is the approach we followed as described in the next section.

5. Connection Between Meandering Channel Morphometry and At-Station Hydraulic Geometry

[28] To study the possible connection between channel planform geometry and at-site HG exponents, we first need to define “representative reaches” upstream of each station. It is noted that the length of the representative reach assigned to each station will depend on the Strahler order of the stream (or the area draining to each station) with stations of, say, order 3 being assigned a smaller representative reach than stations of order 5, and so forth. It is desirable that, on the average, the number of meanders encountered in each representative reach is the same. To accomplish this we used the median planform properties of

streams of different orders as presented in Table 2 (e.g., median sinuosity s_ω and median wavelength λ_ω of stream of order ω) and computed for each order ω the along-valley length of a “median meander bend” as λ_ω/s_ω . The along-valley length of the representative reaches was chosen to be approximately 3 times the along-valley length of the median meander bends, i.e., a length of approximately $3\lambda_\omega/s_\omega$ for a stream of order ω , measured upstream from each station along the valley slope. Since the spatial extent of data set A is much larger than the high-resolution hydrography data of data set B (which was used for the extraction of planform properties of Table 2) additional work was performed to extract planform properties in the regions lacking high-resolution hydrography data. Namely, the channel center line in the vicinity of every station (except the ones in Neosho and Osage river basins – data set B) were digitized from 1:24,000 topographic maps over lengths of approximately $3\lambda_\omega/s_\omega$ according to the order of the channel. Then, the at-station channel sinuosity and average curvature were computed from the digitized lines.

[29] In Figure 10, we plot the at-station HG exponents for velocity versus the at-station sinuosity and normalized channel curvature ($W_{bf}^i \bar{C}^i$, where W_{bf}^i is the bank-full width and \bar{C}^i the average curvature of the representative reach of station i) for the 96 stations of data set A. Clearly, both plots show a dependence of HG on channel planform geometry expressed in terms of a decrease of the exponent m with an increase in sinuosity and normalized curvature. As we have already shown that the sinuosity increases in the downstream direction, the immediate conclusion is that the overall trend in the region of interest is toward a decrease of velocity exponents with an increase in contributing area.

[30] To show that the dependence between HG exponents and sinuosity is due to the increasing channel asymmetry downstream we employed the linear model of meandering rivers of *Johannesson and Parker [1987, 1989]* (see Appendix B for a brief description of the model). *Johannesson and Parker [1987, 1989]* proposed a two-dimensional (longitudinal and transverse coordinates) model for river meandering based on momentum balance, continuity and sediment conservation equations under the

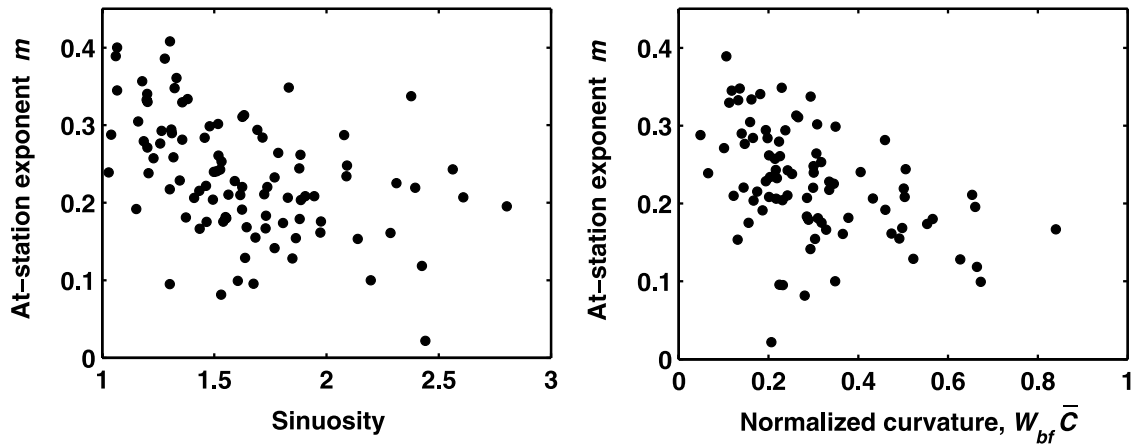


Figure 10. Plots of at-station exponents for velocity (m) as a function of sinuosity and normalized curvature.

assumption of steady slender flow. This model calculates the flow field and bed topography in curved channels with an erodible bed. The coupling between flow field, bed load transport and bed topography was shown in that work to cause significant increase of the lateral bed slope which was not reproduced by previous studies neglecting the convective transport of primary flow momentum by secondary flows in the transverse direction. The governing equations of the model are summarized in Appendix B.

[31] The model of *Johannesson and Parker* [1987] was adopted in our analysis by using it on representative meander bends of various orders ω . By supplying channel bank-full properties for a channel of order ω , i.e., width W_{bf}^ω , average depth D_{bf}^ω , average velocity V_{bf}^ω , channel slope S^ω , meander wavelength λ_ω , angle amplitude Θ_O^ω and a perturbation parameter Ψ_O defined as $\Psi_O = \pi \Theta_O^\omega W_{bf}^\omega / \lambda_\omega$, we can compute, using the model, the bed topography at several cross sections of that meander bend. By using properties of meandering channels of different orders ω (extracted from the region of Neosho-Osage river basins in Oklahoma and Kansas), regional HG relationships can be derived as a function of scale and compared with the empirical ones.

[32] The representative meander bends were chosen to have cross-sectional geometry represented by the power law approximations in Figure 5 (data set A) and median plan-form geometry extracted from the high-resolution hydrography of Neosho and Osage river basins (data set B). In analogy to (6a)–(6b), the perturbation parameter Ψ_{O_ω} was computed as

Median perturbation parameter

$$\Psi_{O_\omega}^{med} = 2.2\pi W_{bf}^\omega \text{Med}\left\{\left[\frac{(s_\omega^i - 1)}{s_\omega^i}\right]^{1/2} / \lambda_\omega^i\right\}. \quad (7)$$

[33] A summary of all the needed parameters for constructing representative meander bends of different orders is given in Table 2 (except the median size of bed material D_{50} , which was assumed to be 1.5 mm, the average for the region of interest, since no trend of downstream fining was observed). Using these parameters in the governing equations of the physical model, the steady state bed topography of representative meander bends was computed for different order streams.

[34] In Figure 11, example cross sections of synthetic bends of streams of order 2 and 7 are shown. Clearly, the trend is toward an increase in transversal slope, and respectively increase in cross section asymmetry with an increase in stream order. Furthermore, the percentage of the along-channel length (or the number of cross sections) significantly affected by asymmetry increases considerably with the stream order. The cross sections with a break in transversal slope (e.g., see Figure 11 for bends of order 7) are those at which the perturbation in channel depth exceeds the mean depth of the channel. In such cases we assume that the secondary currents scour additionally the outer bank, depositing sediment at the inner 2/3 of the channel width, while at the same time preserving the width, mean depth and mean transversal slope of the channel as predicted by the theory (see also Appendix B).

[35] Having the channel cross sections of each synthetic meander bend, a conditional HG was extracted based on the assumption of normal flow at any cross section in the bend and using the Manning-Strickler's power relation for resistance $U/u_* = 8.1(H/k_S)^{1/6}$, where $u_* = \sqrt{gHS}$ is the shear velocity and k_S the effective roughness (estimates of effective roughness were computed for every channel order using this relation and bank-full channel properties given in Table 2, i.e., substituting $H = D_{bf}^\omega$ and $U = W_{bf}^\omega$ and solving for k_S^ω). The HG is called conditional since it represents the expected velocity through the bend, conditional on a given discharge at every cross section as the discharge increases.

[36] Examples of conditional hydraulic geometry for velocity are given in Figure 12 for synthetic meander bends of order 1, 3, 5 and 7. Note that the theoretical HG relationships are slightly nonlinear in the log-log domain as was pointed out by *Ferguson* [1986]. The purpose of their approximation by power laws (the straight lines in Figure 12) in this study is to facilitate the comparison with empirical data in terms of a few parameters, i.e., the preexponents k and the exponents m in these relationships.

[37] In Figure 13 we plot the coefficients k and the exponents m of the predicted (from linear theory) and the empirical at-station HG for velocity as a function of scale (for data set A). For comparison, the predictions of HG based on the multiscale models of discharge and cross-sectional area proposed by *Dodov and Foufoula-Georgiou* [2004] and reviewed in section 2 are also given (i.e., as

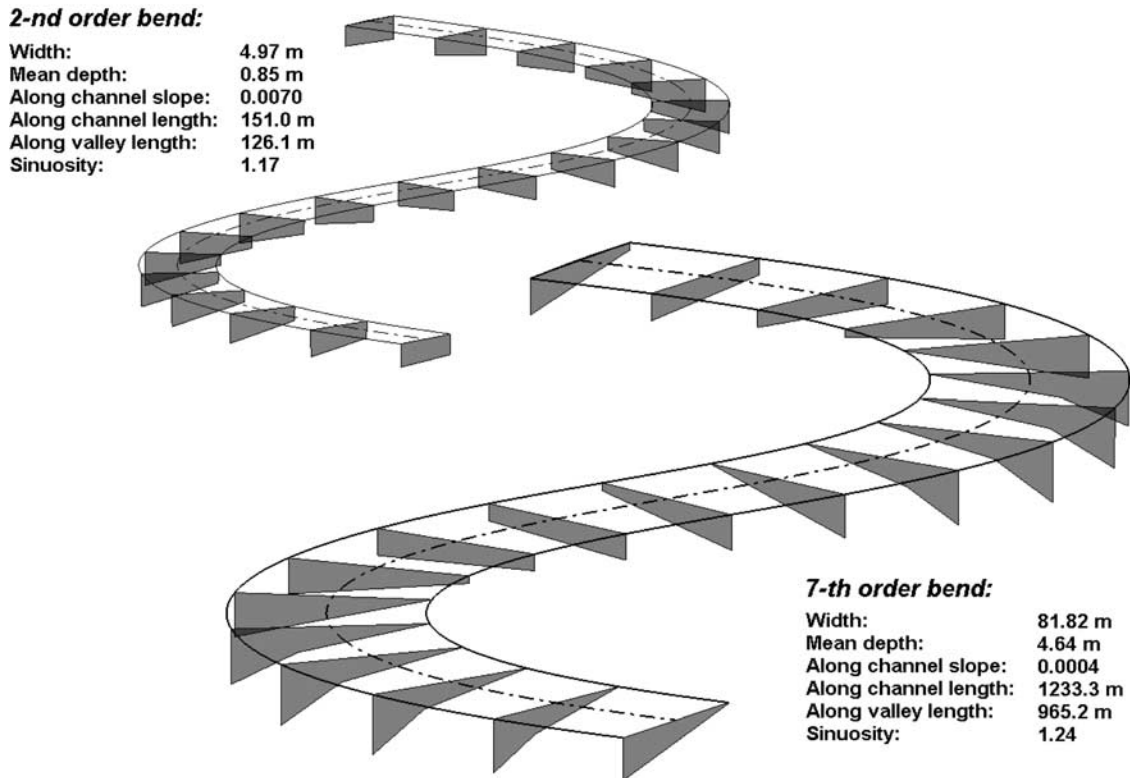


Figure 11. Examples of “synthetic” meandering bends of a given stream order generated from the linear meandering model of *Johannesson and Parker* [1987] using the representative meander bend parameters of Table 2. Examples of second- and seventh-order bends are shown above.

computed from relationships (3c) and (3d) using the parameters of Table 1 fitted to data set A). What is evident from these figures is that independently of the functional type of the decay of HG exponents with scale, the trend of decreasing magnitude of these parameters with scale is well reproduced by both the multiscaling model and the linear theory.

[38] To test the statistical significance of the trend we apply a hypothesis testing with the null hypothesis that the slope of the least squares fit to the relationship m versus $\ln(A)$ is equal to zero. The statistic for this test (under the premise of Gaussian error model [e.g., see *Devore and Peck*, 1996]) is given by the expression

$$t = b \left[\frac{\sum_{i=1}^n (m_i - \hat{m}_i)^2 / (n-2)}{\sum_{i=1}^n (\ln A_i - \overline{\ln A})^2} \right]^{-1/2}, \quad (8)$$

where b is the slope of the linear model fit, \hat{m}_i is the estimate of the linear model fit for a given $\ln A_i$ and n is the number of samples. The computed test statistics is $t = -5.06$ and for 94 degrees of freedom (96 stations - 2), the probability $P(t < -5.06)$ and $P(t > 5.06)$ is $2.04 \times 10^{-4}\%$ (double sided test to check if $b \neq 0$). Since this percent is much less than any reasonable confidence threshold the hypothesis is rejected, i.e., the trend of decrease of exponent m with scale is statistically significant. Although visually minor, this trend has been shown to play an important role when considered in the context of hydrologic response [see *Dodov and Foufoula-Georgiou*, 2004] since it significantly affects the shape of

the hydrograph and implies different degrees of non-linearity in catchment response at different scales.

6. Insights From Contrasting the Statistical and Physical Theories: The Role of Thresholds

[39] A closer examination of Figure 13 suggests some differences in the trends of the exponent m with contributing area predicted from the statistical and physical theories, i.e., for the linear theory a steep decay up to approximately 700 km^2 and almost constant exponents after that, and for the multiscaling theory exponents following almost a straight line with log-area. To explain this difference, let us consider the plots in Figure 14. In these plots we compare the scaling of bank-full discharges Q_{bf} and cross-sectional areas $C_{A,bf} = W_{bf}D_{bf}$ of data set A with the scaling of the empirical quantiles of Q and C_A corresponding to frequencies of exceedance 50% and 5%. The quantiles of Q and C_A were computed directly from observations and nonparametrically, i.e., without assuming any particular distribution for daily discharges and any particular relationship (e.g., power laws) between discharge and cross-sectional area.

[40] It is evident from Figure 14 that the below bank-full empirical log-quantiles of Q and C_A (points) follow almost straight lines with log-area, and are in good agreement with the quantiles predicted by the multiscaling theory (solid lines). This observation supports once again the multiscaling formalism for below bank-full discharges introduced by *Dodov and Foufoula-Georgiou* [2004]. In that study only

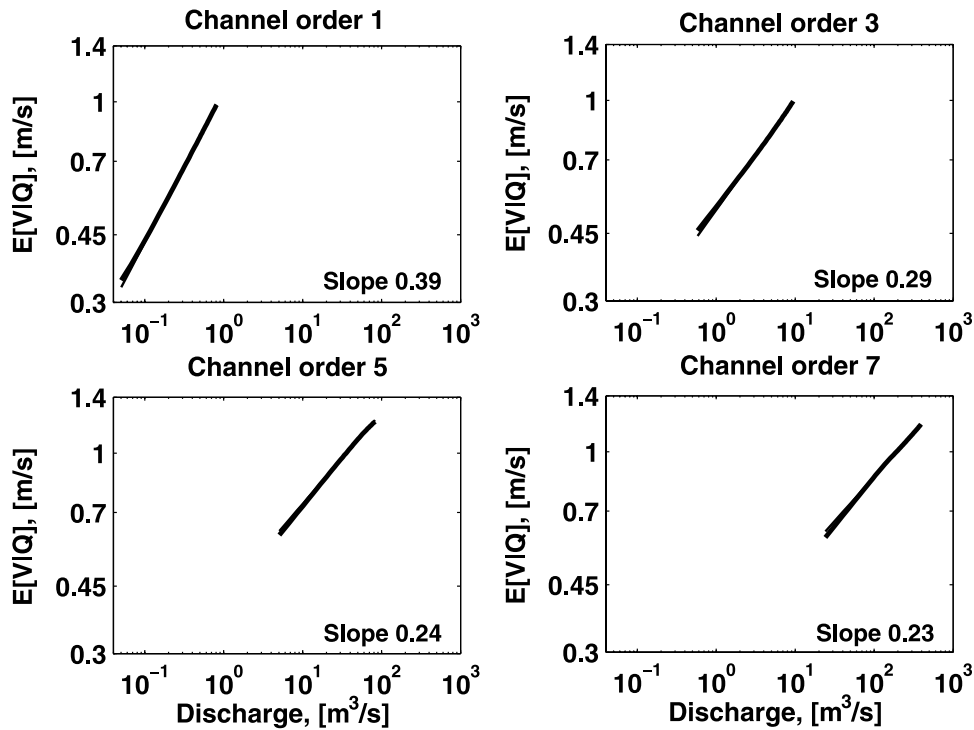


Figure 12. Examples of conditional hydraulic geometry for velocity as computed for synthetic meander bends of different order. Expectation was taken over 20 cross sections of the synthetic meander bends. The straight lines represent the fitted power law approximation of the theoretical relationships.

quantiles corresponding to frequencies of nonexceedance of Q and C_A of up to 99.4% were explicitly considered in the multiscaling model fitting (specifically, ten frequencies of nonexceedance $p = \{0.006, 0.026, 0.082, 0.202, 0.391, 0.609, 0.798, 0.918, 0.974, 0.994\}$), thus neglecting the effect of near-bank and overbank flows whose frequency of nonexceedance is typically larger than 99%. In contrast, hydraulic geometry derived from the linear theory is based on the double power law approximations of channel bank-full morphometry shown in Figure 5 and thus explicitly incorporates a physical threshold of the system and its dependence on scale (i.e., the transition from below to

above bank-full conditions and how this transition changes with scale). This physical threshold is not accounted for in the multiscaling theory of HG. Despite the above explained disagreement between the multiscaling theory and physical theory predicted HG, one could argue that both predictions are acceptable within the scatter of empirical observations, which is considerable especially for large contributing areas (see Figure 13).

[41] It is worth commenting here that the scaling and scaling break of above bank-full flows seen in Figure 14 (left) is expected to be reflected in the scaling of (maximum annual) floods. For river reaches with contributing areas less

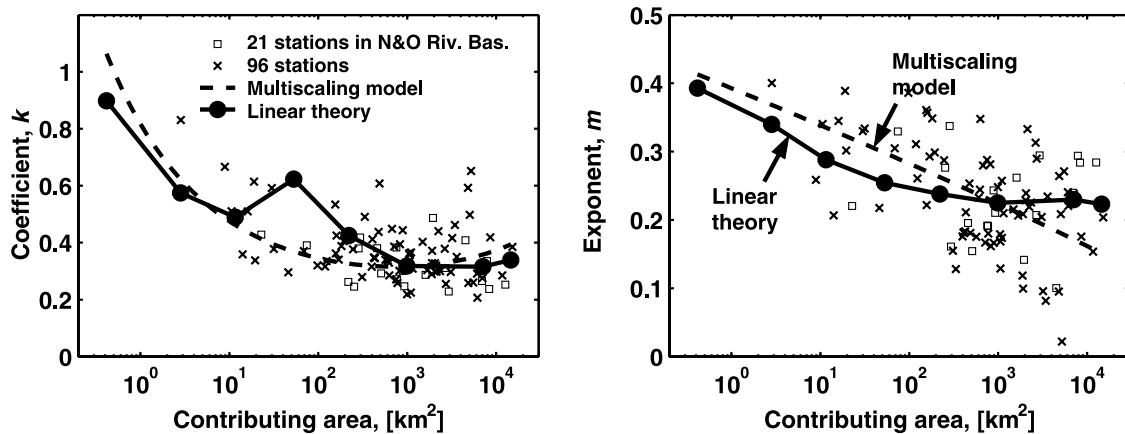


Figure 13. Comparison of theoretical (as predicted from linear meandering theory (solid circles and interpolated solid line) and multiscaling theory (dashed line)) and empirical hydraulic geometry for velocity. The coefficient k and the exponent m in the relationship $V = kQ^m$ are shown, respectively.

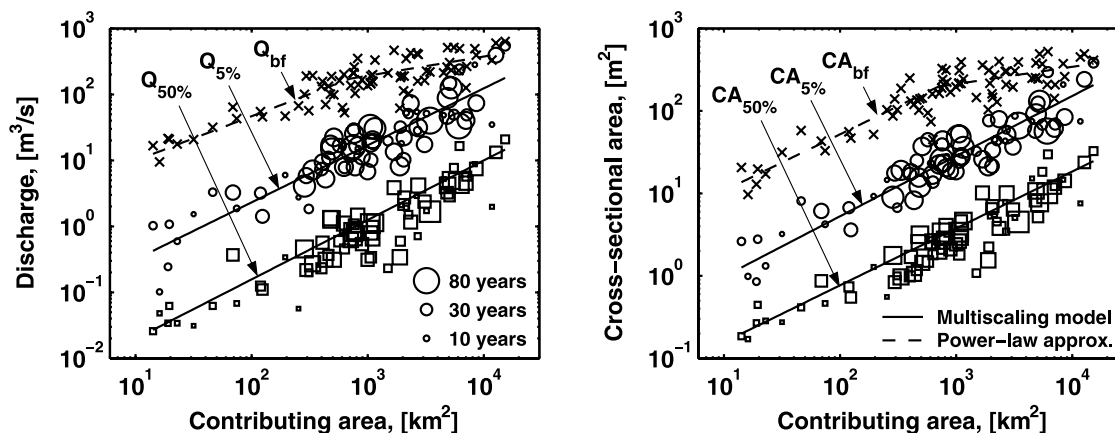


Figure 14. Scaling of discharge and cross-sectional area: comparison of bank-full discharge Q_{bf} and cross-sectional area at bank-full $C_{A_{bf}}$ of data set A (top curves) with the Q and C_A empirical quantiles of frequency of exceedance 50% and 5% based on at least 3 years of unregulated discharge. The predictions of the multiscaling model (solid lines) are also given for the 50% and 5% quantiles and show good agreement with the observations. The crosses for the bank-full properties correspond to the observations, and the dashed lines are least squares fitted (same as the lines of bank-full properties shown in Figure 5).

then 700 km², the frequency of occurrence of overbank flows is almost constant (i.e., parallel lines of Q_{bf} , $Q_{50\%}$ and $Q_{95\%}$, and $C_{A_{bf}}$, $C_{A_{50\%}}$ and $C_{A_{95\%}}$ in Figure 14), while for larger rivers this frequency seems to depend on contributing area (i.e., different slopes of Q_{bf} compared to $Q_{50\%}$ and $Q_{95\%}$, and $C_{A_{bf}}$ compared to $C_{A_{50\%}}$ and $C_{A_{95\%}}$). In other words, river reaches that drain large areas will be more frequently flooded than smaller ones. Considering the retardation effects of overbank storages on peak flows, one could easily guess that the peak flow statistics will be affected in a different way at different scales with a trend of decreasing variability downstream. This observation is revealing and is analyzed in detail in a subsequent publication (B. Dodov and E. Foufoula-Georgiou, Fluvial processes and streamflow variability: Interplay in the scale-frequency continuum and implications for scaling, submitted to *Water Resources Research*, 2004, hereinafter referred to as Dodov and Foufoula-Georgiou, submitted manuscript, 2004) in the context of the so-called multiscaling theory of flood peaks [see Gupta and Waymire, 1990; Gupta et al., 1994; Gupta and Dawdy, 1995].

7. Summary and Conclusions

[42] The relations between channel morphology and discharge (known as hydraulic geometry: HG) are widely used by geomorphologists and hydrologists since their introduction by Leopold and Maddock [1953]. Recently, Dodov and Foufoula-Georgiou [2004] showed that these relationships might deviate from simple power laws with constant exponents as initially proposed. More specifically, they showed that the exponents of the at-site HG systematically depend on upstream contributing area. The authors provided empirical evidence for this scale dependence and proposed a statistical framework (based on a multiscaling formalism) within which these empirical trends could be interpreted and quantified.

[43] In the present paper, we offer a physical explanation of the scale dependence of HG. Using a physically based

theory which connects channel planform geometry (e.g., sinuosity, curvature and meander wavelength) and channel cross-sectional shape under preservation of the momentum, water and sediment [Johannesson and Parker, 1987, 1989], we predict HG and show that the physically derived HG agrees with the empirical trends and to a degree with the statistically predicted HG based on the multiscaling theory. This agreement, together with a parallel analysis of the dependence of channel planform geometry on scale and dependence of at-station HG exponents on sinuosity, is interpreted as evidence that the physical origin of the scale-dependent HG is the systematic increase of channel asymmetry downstream induced by scale-dependent fluvial instability.

[44] It is noted that the systematic change of HG exponents with scale reported herein has been extracted from thousands of streams in a region with overall homogeneous geologic, topographic and hydroclimatic conditions, and thus, for every scale of interest, it reflects the spatially variable planform and channel geometry characteristics present in that region (e.g., see PDFs of sinuosity for a particular scale in Figure 7). In this sense, it is noted that the notion of scaling of at-site HG is to be interpreted in statistical terms (i.e., akin to the scaling and regionalization of floods) and not as the change of HG as one goes downstream along individual reaches of the river.

[45] An interesting observation, namely the dependence of the frequency of occurrence of overbank flow on contributing area, suggests that river reaches that drain large areas are more frequently flooded than smaller ones. This observation also sheds light into the decreasing variability of flood peaks for large areas (considering the retardation effect of overbank storages on peak flows) and is explored in its own right in a subsequent paper (Dodov and Foufoula-Georgiou, submitted manuscript, 2004) in the context of the multiscaling theory of flood peaks [see Gupta and Waymire, 1990; Gupta et al., 1994; Gupta and Dawdy, 1995].

[46] The development of synthetic HG (used in this paper to physically explain the systematic variations of at-station

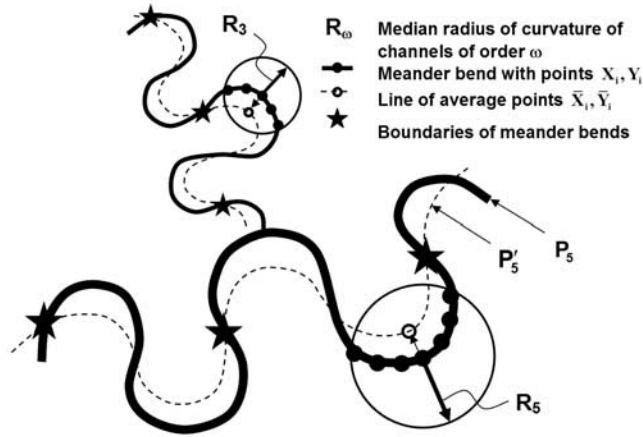


Figure A1. Schematic to illustrate the determination of boundaries of meander bends for the analysis of high-resolution hydrography data. The solid line shows the actual river meander, and the dashed line shows the line of average points.

HG with scale) can be itself a valuable practical tool for runoff-routing applications in ungauged basins. A methodology based on the linear theory of river meandering can be used for computing synthetic HG of individual channels (based on supplied representative values or PDFs of the parameters describing channel planform geometry and cross-sectional morphometry), which can then be applied for distributed probabilistic routing in ungauged catchments. Such an approach would provide realistic bank-full discharges and timely transition to overbank regime, which is very important from both hydrologic and geomorphologic point of view.

Appendix A: Derivation of Meander Bend Properties (Sinuosity, Meander Wavelength, and Radius of Curvature) From High-Resolution Hydrography Data

[47] The available hydrography data is in the form of GIS Arc/Info line coverages. From these data, derivation of meander bend properties is performed at three stages.

[48] 1. At the first stage, the data is first carefully examined to clean all loops and artificial canals and Strahler stream order is assigned to every channel in the river network.

[49] 2. At the second stage, a radius of curvature is assigned to every tree successive points of every polyline representing a channel. The median radius of curvature is then calculated for all triplets of points belonging to a given Strahler order.

[50] 3. At the third stage, for every point (X_i, Y_i) in a polyline P_ω of order ω , another point (\bar{X}_i, \bar{Y}_i) is calculated such that $\bar{X}_i = \sum_{j=1}^m X_j$, $\bar{Y}_i = \sum_{j=1}^m Y_j$, $(X_j, Y_j) \in R_\omega|_{X_i, Y_i}$ where $R_\omega|_{X_i, Y_i}$ is a ball of radius R_ω (the median radius of curvature of a channel of order ω computed at the second stage) centered at (X_i, Y_i) . Thus for every polyline P_ω another polyline P'_ω is computed, consisting of all points (\bar{X}_i, \bar{Y}_i) . The even crossings of the two polylines is then assumed to represent the boundaries of the meander bends as shown in Figure A1. Once the boundaries of

all meander bends are defined, their parameters (sinuosity, meander wavelength and radius of curvature) are easily calculated and statistics over all meander bends of a given order performed.

Appendix B: Implementation of Linear Theory of River Meandering for Derivation of “Synthetic” Hydraulic Geometry

[51] The theory is based on the two dimensional (longitudinal and transversal coordinates) momentum balance, continuity and sediment conservation equations under the assumption of steady slender flow [see *Johannesson and Parker, 1987*]:

Longitudinal momentum balance

$$\bar{T}^2 \left(\frac{1}{1 + \tilde{n}\tilde{C}} \bar{u} \frac{\partial \bar{u}}{\partial \tilde{s}} + \tilde{v} \frac{\partial \bar{u}}{\partial \tilde{n}} + \frac{\tilde{C}}{1 + \tilde{n}\tilde{C}} \bar{u} \tilde{v} \right) = -g \frac{1}{1 + \tilde{n}\tilde{C}} \frac{\partial \tilde{\xi}}{\partial \tilde{s}} - \frac{\tilde{\tau}_s}{\rho \tilde{h}} - \frac{1}{\tilde{h}} \cdot \left\{ \frac{\partial}{\partial \tilde{n}} \left[\tilde{u} \tilde{h} \int_0^1 T \tilde{v} d\zeta \right] + \frac{2\tilde{C}}{1 + \tilde{n}\tilde{C}} \tilde{u} \tilde{h} \int_0^1 T \tilde{v} d\zeta \right\}, \quad (B1)$$

Transversal momentum balance

$$\frac{1}{1 + \tilde{n}\tilde{C}} \bar{u} T \frac{\partial}{\partial \tilde{s}} (\tilde{v} T + \tilde{v}) + (\tilde{v} T + \tilde{v}) \frac{\partial}{\partial \tilde{n}} (\tilde{v} T + \tilde{v}) - \frac{\tilde{C}}{1 + \tilde{n}\tilde{C}} \bar{u}^2 T^2 = -g \frac{\partial \tilde{\xi}}{\partial \tilde{n}} + \nu_t \frac{\partial^2}{\partial \tilde{z}^2} (\tilde{v} T + \tilde{v}), \quad (B2)$$

Continuity equation

$$\frac{\partial \tilde{u} \tilde{h}}{\partial \tilde{s}} + \frac{\partial}{\partial \tilde{n}} [(1 + \tilde{n}\tilde{C}) \tilde{v} \tilde{h}] = 0, \quad (B3)$$

Sediment conservation

$$(1 - p) \frac{\partial \tilde{\eta}}{\partial t} + \frac{1}{1 + \tilde{n}\tilde{C}} \left\{ \frac{\partial \tilde{q}_s}{\partial \tilde{s}} + \frac{\partial}{\partial \tilde{n}} [(1 + \tilde{n}\tilde{C}) \tilde{q}_n] \right\} = 0, \quad (B4)$$

where

- \bar{u}, \bar{v} longitudinal and transverse depth-averaged velocities;
- \tilde{v} transverse velocity;
- $\tilde{s}, \tilde{n}, \tilde{z}$ longitudinal and transverse coordinates and distance upward normal from the bed;
- T dimensionless velocity shape function;
- \tilde{C} curvature of center line;
- $\tilde{h}, \tilde{\eta}, \tilde{\xi}$ upward normal depth, bed elevation, and water surface elevation, $\zeta = \tilde{z}/\tilde{h}$;
- g, ρ, ν_t acceleration due to gravity, fluid density, and eddy viscosity;
- \tilde{q}_s, \tilde{q}_n volumetric sediment transport per unit width in the \tilde{s}, \tilde{n} directions;
- $\tilde{\tau}_s$ bed stress in the \tilde{s} direction;
- p sediment porosity.

[52] After conversion of the above equations to a dimensionless form, they are linearized by expansion for small curvature C in the form

$$(u, v, \eta) = (1, 0, 0) + \Psi_0(u_1, v_1, \eta_1) + \dots, \quad (B5)$$

$$(h, \xi, \eta) = (1, \xi_r - bS/D, \eta_r - bS/D) + \Psi_0(h_1, \xi_1, \eta_1) + \dots, \quad (B6)$$

$$(q_s, q_n) = q_{s0}[(1, 0) + \Psi_0(q_{s1}, q_{n1}) + \dots], \quad (B7)$$

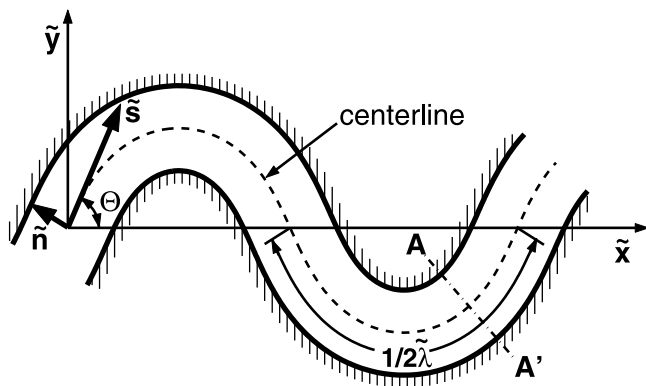


Figure B1. Schematic of a meander bend following a sine-generated curve and definition of variables and coordinate system for the governing equations of the physical model of meandering rivers [from *Johannesson and Parker*, 1989, Figure 1].

where u , v , w , h , ξ , η , q_s and q_n are dimensionless equivalents of \bar{u} , \bar{v} , \bar{w} , \bar{h} , $\bar{\xi}$, $\bar{\eta}$, \bar{q}_s and \bar{q}_n , b is the channel half-width, S is the along-channel slope, D the channel mean depth and ξ_r and η_r are the reference elevations for which $D = \xi_r - \eta_r$. The perturbation parameter Ψ_0 is usually of order $O(10^{-1}$ to $10^{-2})$ and for sinuous channel is defined as $\Psi_0 = b/\tilde{\lambda}$, where $\tilde{\lambda}$ is the meander wavelength (see Figure B1 for a schematic of a meander bend following a sine-generated curve and a definition of the coordinate system and some of the variables).

[53] For the perturbations ξ_1 and η_1 the solutions for a sine-generated curve [see *Langbein and Leopold*, 1966] at $n = 1$ are given as

$$\xi_1 = Fr^2 X_{20} \sin(2\pi s/\tilde{\lambda}) \quad (B8)$$

and

$$\eta_1 = -A \cos \sigma_{SL} \sin(2\pi s/\tilde{\lambda} - \sigma_{SL}) + \tilde{A}_F \cos(2\pi s/\tilde{\lambda}) + \tilde{B}_F \sin(2\pi s/\tilde{\lambda}), \quad (B9)$$

where

Fr	Froude number at bank-full;
X_{20} , \tilde{A}_F , \tilde{B}_F	parameters;
A	bed score factor;
σ_{SL}	phase shift of secondary flow.

[54] Given the linearity of the solution, the bed topography is uniquely defined once $\xi_1(n = 1)$ and $\eta_1(n = 1)$ are computed. Technical details about the assumptions made, parameter estimation and implementation of the model can be found by *Johannesson and Parker* [1987, 1989].

[55] Some additional assumptions are made in our implementation.

[56] 1. Meander bends are represented by sine-generated curves with minimum radius of curvature computed by means of (6b);

[57] 2. The critical Shield stress for all stream orders is assumed $\tau_c^* = 0.047$;

[58] 3. In the case when the perturbation in channel depth exceeds the mean depth (a problem that is considered by the authors of the theory as a drawback (G. Parker, personal

communication, 2003) we assume that the secondary currents scour additionally the outer bank, depositing sediment at the inner 2/3 of the channel width, while at the same time preserving the width, mean depth and mean transversal slope of the channel predicted by the theory.

[59] **Acknowledgments.** This research is jointly funded by NSF (under grant EAR-0120914) as part of the National Center of Earth Surface Dynamics (NCED) at the University of Minnesota and by NASA's Land Surface Hydrology Program under grant NAG8-1519. Computer resources were provided by the Minnesota Supercomputing Institute (MSI). We thank Gary Parker and Chris Paola for insightful discussions and encouragement during the course of this study. Special thanks go also to James Putnam and Bob Tortorelli from the USGS offices in Kansas and Oklahoma for providing us with large number of station-specific data. The critical comments of an anonymous referee resulted in additional analysis which strengthened our conclusions and interpretations.

References

- Callander, R. A. (1969), Instability and river channels, *J. Fluid Mech.*, *36*, 465–480.
- Devore, J., and R. Peck (1996), *Statistics: The Exploration and Analysis of Data*, 3rd ed., 852 pp., Duxbury, Boston, Mass.
- Dodov, B., and E. Foufoula-Georgiou (2004), Generalized hydraulic geometry: Derivation based on a multiscale formalism, *Water Resour. Res.*, *40*, W06302, doi:10.1029/2003WR002082.
- Ferguson, R. (1986), Hydraulics and hydraulic geometry, *Prog. Phys. Geogr.*, *10*, 1–31.
- Gupta, V. K., and D. Dawdy (1995), Physical interpretation of regional variations in the scaling exponents in flood quantiles, *Hydrol. Processes*, *9*, 347–361.
- Gupta, V. K., and E. Waymire (1990), Multiscale properties of spatial rainfall and river flow distributions, *J. Geophys. Res.*, *95*, 1999–2009.
- Gupta, V. K., O. J. Mesa, and D. R. Dawdy (1994), Multiscale theory of flood peaks: Regional quantile analysis, *Water Resour. Res.*, *30*, 3405–3421.
- Hansen, E. (1967), The formation of meanders as a stability problem, *Basic Res. Prog. Rep. 13*, Hydraul. Lab., Tech. Univ. of Denmark, Kgs. Lyngby.
- Ikeda, H. (1989), Sedimentary controls on channel migration and origin of point bars in sand-bedded meandering rivers, in *River Meandering*, *Water Resour. Monogr.*, vol. 12, edited by S. Ikeda and G. Parker, pp. 51–68, AGU, Washington, D. C.
- Johannesson, H., and G. Parker (1987), Theory of river meanders, *Proj. Rep. 278*, St. Anthony Falls Hydraul. Lab., Univ. of Minn., Minneapolis.
- Johannesson, H., and G. Parker (1989), Linear theory of river meandering, in *River Meandering*, *Water Resour. Monogr.*, vol. 12, edited by S. Ikeda and G. Parker, pp. 181–214, AGU, Washington, D. C.
- Juracek, K. E. (1999), Channel stability of the Neosho River downstream from John Redmond Dam, Kansas, *U.S. Geol. Surv. Fact Sheet*, *088-99*, 4 pp.
- Juracek, K. E. (2000), Channel stability downstream from a dam assessed using aerial photographs and stream-gage information, *J. Am. Water Resour. Assoc.*, *36*, 633–645.
- Langbein, W. B., and L. B. Leopold (1966), River meanders—Theory of minimum variance, *U.S. Geol. Surv. Prof. Pap.*, *422-H*, 1–15.
- Leopold, L. B., and T. Maddock (1953), The hydraulic geometry of stream channels and some physiographic implications, *U.S. Geol. Surv. Prof. Pap.*, *252*, 57 pp.
- Leopold, L. B., and M. G. Wolman (1957), River channel patterns: Braided, meandering, and straight, *U.S. Geol. Surv. Prof. Pap.*, *282-B*, 85 pp.
- Leopold, L. B., and M. G. Wolman (1960), River meanders, *Bull. Geol. Soc. Am.*, *71*, 769–794.
- Parker, G. (1976), On the cause and characteristic scales of meandering and braiding in rivers, *J. Fluid Mech.*, *76*, 457–480.
- Schumm, S. A., and H. R. Khan (1972), Experimental study of channel patterns, *Geol. Soc. Am. Bull.*, *83*, 1755–1770.
- Stall, J. B., and Y. S. Fok (1968), Hydraulic geometry of Illinois streams, *Ill. Water Resour. Res. Rep.*, *15*, 47 pp.

B. Dodov and E. Foufoula-Georgiou, St. Anthony Falls Laboratory, Department of Civil Engineering, University of Minnesota, Mississippi River at 3rd Avenue SE, Minneapolis, MN 55414, USA. (dodo0001@tc.umn.edu; efi@umn.edu)